Modelling of heat transfer in waterjet guided laser drilling of silicon

C-F Li, D B Johnson and **R Kovacevic***
Research Center for Advanced Manufacturing, Mechanical Engineering Department, Southern Methodist University, Richardson, Texas, USA

Abstract: Waterjet guided laser processing is an internationally patented technique based on guiding a laser beam inside a thin, high-speed waterjet. The process combines the advantages of laser processing with those of waterjet cutting. It is very suitable in processing thin and heat-sensitive materials with a high degree of precision required. A model and simulation method for waterjet guided laser drilling on a silicon substrate are presented in this study. A finite difference method has been developed to simulate the thermal field and phase changes involved. The model represents the thermal process in detail. The simulation results predict the main characteristics of waterjet guided laser drilling. The study gives insight into the interactions between the laser beam, waterjet and workpiece material during drilling of a silicon substrate.

Keywords: modelling, waterjet, laser drilling, silicon substrate

NOTATION

A	heat source term (W/m^3)
A_L	heat source term when latent heat is being absorbed or evolved (W/m^3)
c_p	specific heat (J/kg K)
d	diameter of waterjet (laser beam) (m)
d_m	maximum hole depth (m)
$\boldsymbol{e}_z$	unit vector parallel to the z axis
f	pulse frequency (cycles/s)
h_c	convection heat transfer coefficient (W/m^2 K)
I	laser power intensity (W/m^2)
k	thermal conductivity (W/m K)
L	thickness (m)
L_m	latent heat of melting (J/kg)
$\boldsymbol{n}$	unit vector normal to the surface
p	waterjet pressure (N/m^2)
P	laser pulse output (W)
Pr	Prandtl number
q	heat flux (W/m^2)
Q_m	excess heat sum for a particular element (J/m^3)
R	reflectivity of the material
Re	Reynolds number
t	time (s)
t_m	time at which the maximum hole depth is reached (s)
T	temperature (K)
T_a	ambient temperature (K)
T_{im}	imaginary temperature (K)
T_m	melting temperature (K)
T_{re}	real temperature in the hole (K)
V	waterjet speed (m/s)
x, y, z	Cartesian system coordinates (m)
α	absorption coefficient (m^{-1})
ε	local surface emissivity
μ	dynamic viscosity (kg/m s)
ρ	density (kg/m^3)
σ	Stefan–Boltzmann constant
τ	pulse length (s)
φ	pressure loss coefficient

The MS was received on 29 August 2002 and was accepted after revision for publication on 3 January 2003.
**Corresponding author: Research Center for Advanced Manufacturing, Mechanical Engineering Department, Southern Methodist University, 1500 International Parkway, Suite 100, Richardson, TX 75081, USA.*

1 INTRODUCTION

Since its invention in 1960, the laser has found diverse applications in engineering and industry because of its ability to produce high-power beams. In the field of metal processing, laser applications include welding, drilling, cutting, scribing, machining, heat treatment, cladding and alloying. In other fields, such as medical surgery, lasers are also used extensively.

The main advantages of laser cutting over mechanical cutting have been its great flexibility, high precision, high

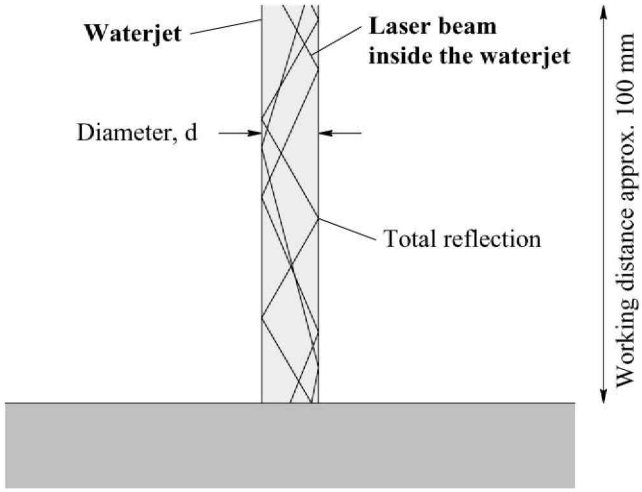

Fig. 1 Schematic mechanism for a waterjet to guide a laser beam (from reference [**1**])

speed and small kerf width with a very narrow heat affected zone. These advantages were expected to provide a solution for dicing silicon wafers in the semiconductor industry. Although silicon is a good candidate for cutting by a laser beam because it absorbs the radiation of the laser beam, lasers have failed repeatedly in the wafer dicing process, largely on account of the collateral thermal damage they produce, including occurrences of crack formation, chipping and deposits of silicon slag.

In 1993, scientists at the Institute for Applied Optics at the Lausanne University of Technology in Switzerland succeeded in creating a waterjet guided laser beam called Microjet [**1**, **2**]. The laser beam is focused in a nozzle while passing through a pressurized water chamber. The geometry of the chamber and nozzle are critical to coupling the energy of the laser beam to the waterjet. The low-pressure waterjet emitted from the nozzle guides the laser beam by means of total reflection at the water–air interface, because of the difference in the index of refraction of water and air, in a manner similar to conventional optical fibres (see Fig. 1). Thus, the waterjet can be described as a fluid optical waveguide of variable length. The stable length of the waterjet is primarily a function of the pressure and nozzle diameter, and generally 100 mm can be obtained.

A waterjet guided laser beam combines the advantages of both waterjet and laser cutting. However, the physical phenomena involved in processing by the waterjet guided laser beam are not fully understood. So far, no theoretical research has been done on this topic. Understanding the physical phenomena is essential for improving the performance and quality of waterjet guided laser processing. A good understanding of the narrow heat affected zone during the operation is needed to determine the necessary laser parameters, especially for dealing with thin and heat-sensitive materials.

In this process, the laser beam heats and melts the material, and the waterjet guides the laser beam, cools the material during processing and expels the liquefied material. In order to study the complex mechanisms involved in cutting and/or ablating by a waterjet guided laser beam, two approaches could be used. One is experimental observation, and the other is modelling and simulation. It is difficult to observe the interior flow of the molten pool and make clear the effect that the waterjet has on the cooling and expulsion of the molten metal by experiments only. Therefore, the best way is to combine these two methods.

There has been extensive research on the modelling of laser material processing, including laser drilling, cutting and scribing. Most modelling work has involved numerical simulation, since useful analytical solutions are not available for moving boundary problems of this type caused by phase change. Most theoretical analyses and models in the literature [**3**–**8**] are based on a one-dimensional steady state assumption, and three-dimensional transient models are limited [**9**–**14**].

A model and simulation method for waterjet guided laser drilling on a silicon substrate are presented in this study. Parameters involved have been numerically investigated to study their effects on the process. In particular, the waterjet cooling effect and heat affected zone have been studied by evaluating the temperature distribution.

2 THE MODEL

The workpiece is a plate of thickness L, and its top surface lies initially in the $z = 0$ plane. The plate is exposed at time $t = 0$ to the waterjet guided laser. Figure 2 schematically illustrates the coordinate system and mesh array. The model is based on the following assumptions:

1. The laser energy flux is assumed to be uniform inside the diameter of the waterjet. Because of the difference in the index of refraction of water and air, the laser beam is totally reflected at the air–water interface and is therefore contained within the waterjet as a parallel beam, similar to an optical fibre in principle. From this point of view, after many reflections, the laser power intensity will be of uniform distribution along the cross-section of the waterjet, instead of the widely used Gaussian distribution assumption in traditional laser processing. Although somewhat unrealistic for conventional laser processing, a uniform laser power intensity has been used to model, for instance, excimer laser pulses for a simplified one-dimensional configuration [**15**]. Specifically owing to waterjet and laser interaction, a uniform laser power intensity is a realistic assumption for waterjet guided laser processing.
2. Owing to the 'high cooling effect' of the waterjet, the material is assumed to be heated only to the melting

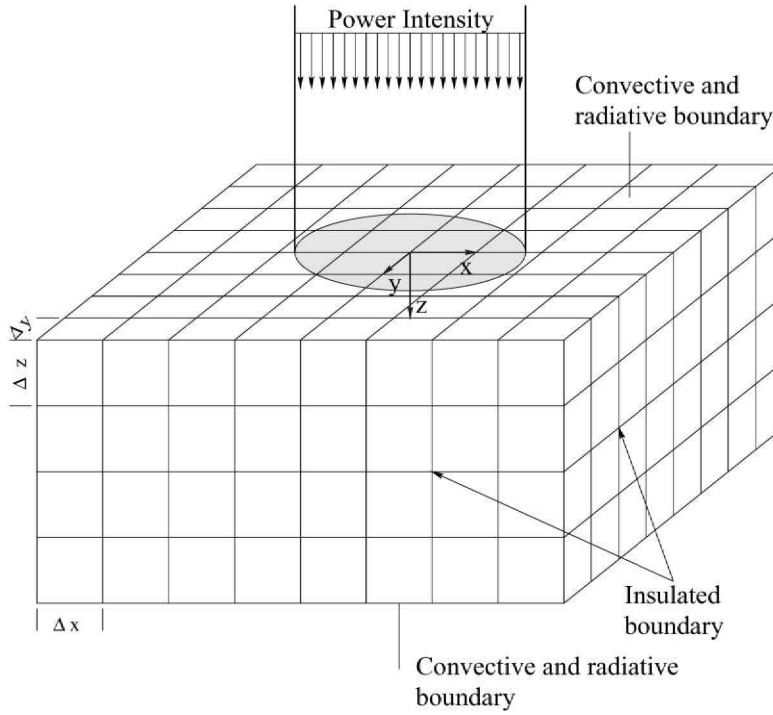

Fig. 2 Schematic depiction of coordinates and boundary conditions

temperature. After an element of the material has reached the melting temperature and also has absorbed incoming energy that exceeds the latent energy of melting, the element melts and is removed by the action of the waterjet.

3. The melting and removal of material is assumed to take place in an element-by-element way. When a particular element reaches the melting temperature and the incoming energy exceeds the latent energy of melting for this element, this part of the material is assumed to be removed by the waterjet and is no longer considered.
4. The flowfield within the molten layer and its effect on heat transfer within the workpiece is neglected since the molten material flows between two almost parallel isothermal surfaces, perpendicular to the enthalpy and temperature gradients.
5. The temperature-dependent thermal properties are considered. The large temperature gradient generated by the intensive laser heat source results in significant thermal property variations. Both thermal conductivity, k, and specific heat, c_p, are often quite strong functions of temperature, particularly in semiconductors such as silicon. Thus, the laser processing will be largely influenced by material temperature-dependent properties. In the present study, two temperature-dependent properties of silicon, heat conductivity k and heat capacity c_p, are modelled as functions of temperature, T, as follows [**16**, **17**]:

$$k(T) = \frac{A}{T \cdot B} \text{ (W/m K)} \tag{1}$$

where $A = 29\,900$, $B = 99$, T is expressed in K and

$$\rho c_p(T) = \left(1.4743 + \frac{0.17066T}{300}\right) \times 10^6 \text{ J/m}^3\text{ K} \quad \text{for } T < 1683\text{ K} \tag{2a}$$

$$\rho c_p(T) = 2.432 \times 10^6 \text{ J/m}^3\text{ K} \quad \text{for } T > 1683\text{ K} \tag{2b}$$

The density variations are comparatively small, and a constant density value of $\rho = 2330\text{ kg/m}^3$ is used.

6. Optical parameters such as surface reflectivity and absorption coefficient also change with temperature, state and laser–material interactions. For this special waterjet guided laser configuration, a detailed discussion of optical parameters is contained in section 4.

3 GOVERNING EQUATIONS AND NUMERICAL FORMULATION

To evaluate the evolution of the temperature field and the propagation of the hole boundary, the time-dependent heat conduction equation is solved in the workpiece domain subject to the assumed boundary conditions. The governing equation is written in terms of temperature T as

$$\frac{\partial(\rho c_p T)}{\partial t} = \nabla \cdot [k(T)\nabla T] + A + A_{\text{L}} \tag{3}$$

where ρ is the density of the material, c_p is the heat

capacity of the material, t is the temporal variable, k is the heat conductivity, A is the heat source term being externally injected or extracted and A_L appears as a heat source term when latent heat is being absorbed or evolved.

For a three-dimensional Cartesian system exhibiting orthotropic symmetry, equation (3) can be written as

$$\frac{\partial(\rho c_p T)}{\partial t} = \frac{\partial}{\partial x}\left[k_x(T)\frac{\partial T}{\partial x}\right] + \frac{\partial}{\partial y}\left[k_y(T)\frac{\partial T}{\partial y}\right] + \frac{\partial}{\partial z}\left[k_z(T)\frac{\partial T}{\partial z}\right] + A + A_L \tag{4}$$

An explicit solution scheme is chosen, using a central difference equation for the spatial derivatives and a forward difference equation for the time advance. The temperature of a given volume element after a specific time step is therefore found explicitly from the known current temperature of the element and its neighbours without the need for any iteration. Short-time increments are required for explicit schemes in order to obtain stability and accuracy. However, explicit schemes may still be preferable to fully or partially implicit ones for simulations such as laser drilling, grooving and cutting, which involve very high thermal gradients and rapidly moving boundaries, since implicit schemes may suffer from convergence failure under these conditions. The stability limit for this explicit scheme is [**18**, **19**]

$$1 - \left[\frac{2k_x}{\rho c_p(\Delta x)^2} + \frac{2k_y}{\rho c_p(\Delta y)^2} + \frac{2k_z}{\rho c_p(\Delta z)^2}\right]\Delta t \geqslant 0 \tag{5}$$

For homogeneous material and a uniform grid, this criterion can be written simply as

$$\Delta t \leqslant \frac{\rho c_p(\Delta x)^2}{6k} \tag{6}$$

Because of the temperature-dependent heat conductivity $k(T)$, careful attention must be paid to the treatment of the conduction term $\nabla \cdot [k(T)\nabla T]$ in order to satisfy energy conservation. Consider the treatment of the term $(\partial/\partial x)[k_x(T)\,\partial T/\partial x]$ as an example. The grid points and cell surfaces are shown in Fig. 3. In finite difference form, $(\partial/\partial x)[k_x(T)\,\partial T/\partial x]$ can be written using three consecutive grid points x_{i-1}, x_i, x_{i+1} as

$$\frac{\partial}{\partial x}\left[k(T)\frac{\partial T}{\partial x}\right]_i = \frac{k_{i+1/2}\dfrac{T_{i+1} - T_i}{x_{i+1} - x_i} - k_{i-1/2}\dfrac{T_i - T_{i-1}}{x_i - x_{i-1}}}{x_{i+1/2} - x_{i-1/2}} \tag{7}$$

It can be seen that two values of the heat conductivity, $k_{i+1/2}$ and $k_{i-1/2}$, have been introduced. The heat flux $q_{i-1/2}$ from x_i to x_{i-1} is $k_{i-1/2}(T_i - T_{i-1})/(x_i - x_{i-1})$, which also can be expressed as

$$q_{i-1/2} = \frac{T_i - T_{i-1}}{(x_i - x_{i-1/2})/k_i + (x_{i-1/2} - x_{i-1})/k_{i-1}} \tag{8}$$

Under uniform grids, equation (8) yields

$$k_{i-1/2} = \frac{2k_{i-1}k_i}{k_{i-1} + k_i} \tag{9}$$

which has been called harmonic averaging [**19**, **20**]. In the present simulation with a non-uniform thermal conductivity distribution, the heat flux across the face between two finite difference cells is calculated by using harmonic averaging, rather than by using arithmetic averaging, so that energy conservation is guaranteed.

4 BOUNDARY CONDITIONS

4.1 Heat injection from the laser beam

The time-dependent laser pulse output $P(t)$ is sketched in Fig. 4, where τ is pulse length and f is pulse frequency. A rectangular wave shape distribution is assumed: pulse output is maximum during the pulse length and sharply decreases to zero out of the pulse length. After $1/f$ time, another pulse occurs.

The laser power intensity is $I(t) = P(t)/(\pi d^2/4)$, where d is the diameter of the waterjet (laser beam). The spatial distribution of the laser power intensity $I(t)$ is considered to be uniform inside the diameter of the waterjet. With the distance z measured from the surface, the volume heat source, $A(z, t)$, is defined as

$$A(z,t) = I(t)[1 - R(T)]\alpha(T)\,\mathrm{e}^{-\alpha(T)z}[\boldsymbol{n}\cdot\boldsymbol{e}_z] \tag{10}$$

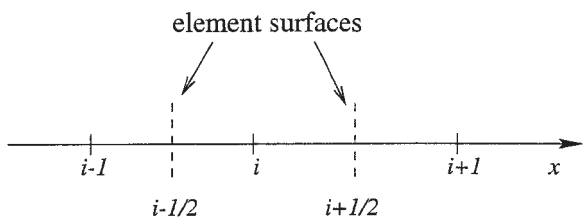

Fig. 3 Grid points in the x direction

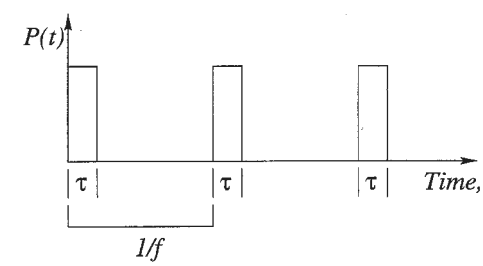

Fig. 4 Laser pulse output

where α is the absorption coefficient, R is the reflectivity of the material, $\boldsymbol{n}$ is a unit vector normal to the surface and $\boldsymbol{e}_z$ is a unit vector parallel to the z axis. Considering multiple reflections of laser radiation within the waterjet, like those in a hole or cavity, the final reflectivity will tend to zero. This means that the laser energy has been nearly totally absorbed by the silicon substrate. Independent of the reflectivity of the material, the assumption that laser energy is totally absorbed by the material is a good approximation in waterjet guided laser processing. Consequently, the difficulty of obtaining a reliable temperature-dependent absorptivity model is avoided, and the volume heat source can be expressed as

$$A(z,t) = I(t)\alpha(T)\,\mathrm{e}^{-\alpha(T)z}[\boldsymbol{n}\cdot\boldsymbol{e}_z] \tag{11}$$

The calculation begins with the assumption of a volumetric heat source according to the preceding equation. The silicon material absorption coefficient will increase greatly when the surface material reaches the melting temperature. Therefore, a change from a volumetric to a surface heat source is assumed for a surface element when its temperature reaches the melting point. Then, the laser heat injection is simply modelled as a surface heat flux

$$q|_{z=0} = I(t)[\boldsymbol{n}\cdot\boldsymbol{e}_z] \tag{12}$$

4.2 Top and bottom surfaces

Convective and radiative heat losses take place at the top and bottom surfaces, and the boundary conditions are

$$I_{\mathrm{loss}} = h_{\mathrm{c}}(T - T_{\mathrm{a}}) + \varepsilon\sigma(T^4 - T_{\mathrm{a}}^4) \tag{13}$$

where h_{c} is the convection coefficient, T_{a} is the ambient temperature, σ is the Stefan–Boltzmann constant and ε is the local surface emissivity. These heat losses are expected to be small, but they are taken into account to maintain the generality of the solution.

4.3 Lateral boundaries

The lateral limits of the domain are taken to be insulating (since the workpiece is generally only a small part of a larger specimen), so that they are assumed to be beyond the regime that is significantly heated during the period of interest.

4.4 Cooling by the waterjet

One of the most important characteristics of waterjet guided laser processing is the high cooling effect performed by the waterjet. Some people have even called the processing 'cool operator' or 'cold laser beam'. Many studies can be found in the literature for jet heat transfer, but mostly for a gas jet and few for a waterjet. Owing to the influence of many factors, fluid jet heat transfer results are not generalized and instead represent special cases and conditions.

For example, in the development of a heat transfer model for continuous-wave (c.w.) laser material processing with gas jet assist [**21**], the convection heat transfer coefficient, h_{c}, was taken as the empirical formula obtained from early experiments by Gardon and Cobonpue [**22**]:

$$h_{\mathrm{c}} = 13Re^{0.5}Pr^{0.33}\frac{k}{B} \tag{14a}$$

which can be expressed in non-dimensional form as

$$Nu_{\mathrm{d}} = \frac{h_{\mathrm{c}}d}{k} = 13Re^{0.5}Pr^{0.33}\frac{d}{B} \tag{14b}$$

where B is the jet plate distance, Re is the Reynolds number at jet exit, Pr is the Prandtl number and k is the thermal conductivity of the gas. In the experiment of Elison and Webb [**23**], the data revealed that the stagnation Nusselt number is nearly independent of the nozzle–plate spacing. This observation is consistent with the conclusion of the experimental study of liquid jets at much higher Reynolds numbers by Stevens and Webb [**24**]. In the experiment of Sun *et al.* [**25**] it was observed that the stagnation heat transfer rate declines with increasing nozzle–plate spacing, but very slightly.

In a review article by Webb and Ma [**26**], many experiments and empirical formulae were summarized. They suggested that the stagnation Nusselt number depends approximately on Pr^n, where n varies between 1/2 at small Prandtl number to 1/3 at large Prandtl number. They recommended that

$$Nu_{\mathrm{d}} = 0.715Re^{1/2}Pr^{0.4} \qquad \text{for } 0.15 < Pr < 3 \tag{15a}$$

and

$$Nu_{\mathrm{d}} = 0.797Re^{1/2}Pr^{1/3} \qquad \text{for } Pr > 3 \tag{15b}$$

They also pointed out that, in the high and moderate Reynolds number range (and for sufficiently high-speed jets), the transport under free-surface liquid jets is relatively insensitive to nozzle–plate spacing. Considering the situation in the present waterjet guided laser processing, equation (15) is a suitable expression for the waterjet cooling effect. For liquid water ranging from 0 to 100 °C, the Prandtl number is from about 13.0 down to 1.7. Since the heating of the specimen is confined to the stagnation zone, the heat transfer in the radial flow regions is negligible assuming that the waterjet and the specimen initially are at the same temperature. Consequently, it is not necessary to know the Nusselt number in the radial flow regions.

4.5 Melting process and material removal

When the specimen absorbs enough laser energy, the temperature arrives at the melting point and the material

starts melting. Melting is accompanied with large latent heat transformation, which will in general strongly affect the heat flow pattern. In the model, the latent heat of melting is treated as a source term and handled by a heat accumulation technique.

After every time step, the temperature of an element exceeding the melting temperature point is reduced to that temperature, and the excess heat is added to an accumulating sum for the element concerned. Once this sum reaches the level needed to melt the element, the transformation is allowed to occur; this element is removed from further calculation, and the new front surface goes to the next element (according to assumption 3). The melting routine can be expressed mathematically as

$$Q_{\mathrm{m}} = \sum_{n_1 \Delta t}^{n_2 \Delta t} \rho c_p (T_{i,j,k} \cdot \ T_{\mathrm{m}}) \tag{16}$$

where Q_{m} is the excess heat sum for a particular element, T_{m} is the melting temperature and $n_1 \Delta t$ is the time at which the melting temperature is first reached. At some later time, $n_2 \Delta t$, the sum Q_{m} reaches the latent heat of melting for the element, L_{m}, melting is assumed to be finished and the element is assumed to be removed by the action of the waterjet.

As melted material is removed, a hole is formed in the substrate. The hole will deepen during the processing, so the hole surface is a moving boundary. On the hole surface, the convection boundary condition is applied. In order to be convenient for computing, a special technique is used to transform the convection boundary condition to the conductive diffusion form, as sketched in Fig. 5 for the one-dimensional case in the x direction.

According to Fourier's law of heat conduction and Newton's law of cooling, the heat transfer balance across the surface is determined by

$$\cdot \ k \frac{\partial T}{\partial x}\bigg|_{\mathrm{wall}} = h_{\mathrm{c}} (T_i \cdot \ T_{\mathrm{re}}) \tag{17}$$

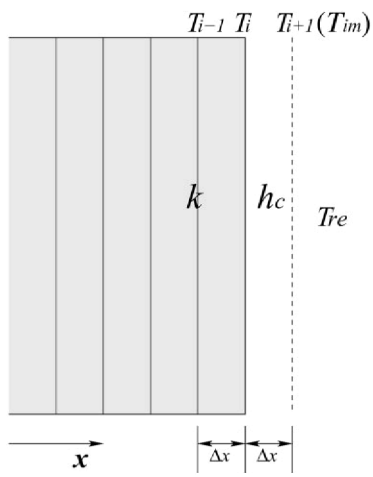

Fig. 5 Imaginary temperature $T_{\mathrm{im}} = T_{i+1}$

where T_{re} is the real temperature in the hole. The finite difference expression for the derivative can be written as

$$\cdot \ k \frac{\partial T}{\partial x}\bigg|_{\mathrm{wall}} = k \frac{T_i \cdot \ T_{i+1}}{\Delta x}$$

If the hole is to the right of the element, there is no material at $i+1$, and T_{i+1} is referred to as the imaginary temperature, T_{im}. Thus, the finite difference form of the heat transfer balance is

$$k \frac{T_i \cdot \ T_{\mathrm{im}}}{\Delta x} = h_{\mathrm{c}} (T_i \cdot \ T_{\mathrm{re}}) \tag{18}$$

An expression for T_{im} can be found by rearranging the above equation, which leads to

$$T_{\mathrm{im}} = T_i \cdot \ \frac{h_{\mathrm{c}} \Delta x}{k} (T_i \cdot \ T_{\mathrm{re}}) \tag{19}$$

where $h_{\mathrm{c}} \Delta x / k$ is called the Biot number [**18**]. Therefore, the convection boundary condition is used to determine an expression for $T_{\mathrm{im}} = T_{i+1}$ which is required for the solution of the temperature diffusion equation. As the solution proceeds and the hole is created, convection boundary conditions are applied as needed to develop expressions for temperatures at points just outside the changing boundary of the hole.

5 RESULTS AND DISCUSSION

5.1 Comparison of numerical results for the pulsed laser heating of aluminium

The new method developed in this study was used to simulate the pulsed laser heating of aluminium (with no waterjet). The results were compared with those of Diniz Neto and Lima [**11**] in order simply to provide a check on the validity of the transient heat transfer simulation. The evolution of the transient temperature profiles in a 10 μm thick pulsed laser heated aluminium sample was simulated. The temperature-dependent coupling between the laser pulse and the sample and the temperature dependent thermal characteristics of the sample were fully accounted for. All parameters were the same as those used by Diniz Neto and Lima [**11**]. The laser power intensity was distributed both temporally and spatially. In general, the present results are in close agreement with those presented by Diniz Neto and Lima, except that the present temperature values are somewhat high in the whole area. These small differences are believed to be due to the use of different numerical methods, with an explicit scheme used in the present study and the implicit Crank–Nicolson scheme used by Diniz Neto and Lima.

It was observed that, if the laser energy is treated as a volume heat source in the calculations, the value of Δz must be very small, less than the absorption length, to

give accurate results. For aluminium, the absorption coefficient $\alpha = 10^8\,\mathrm{m}^{-1}$, which means that the absorption length $1/\alpha = 10^{-8}\,\mathrm{m}$. Owing to the stability limitation for the explicit scheme, the time increment Δt must be extremely small (of the order of $10^{-14}\,\mathrm{s}$). This requires a huge amount of time steps and a quite long running time to compute the solution. Therefore, an explicit scheme is not a good choice for the laser heating of a metal such as aluminium with a very large absorption coefficient, especially if the laser energy input is treated as a volume heat source.

Another way to model the laser and material interaction is to consider the laser light to be fully absorbed by the surface elements. Under this assumption, good results can be obtained when the value of Δz is an order of magnitude ($10^{-7}\,\mathrm{m}$) larger than the absorption length. An increase by an order of magnitude in Δz leads to a significant reduction in the number of time steps and the running time.

Since the absorption coefficient of silicon is only $5.0 \times 10^3\,\mathrm{m}^{-1}$, the associated absorption length is 0.2 mm. Consequently, the values used for Δz and Δt can be approximately 5 orders of magnitude larger for silicon than for aluminium.

5.2 Simulation study of the waterjet guided laser drilling of silicon

Using the new simulation method, a detailed study was made of the waterjet guided laser drilling of silicon. The silicon substrate is assumed to be 320 μm thick. The working conditions are: pulse length 0.08 ms, frequency 1000 Hz, waterjet pressure 50 bar and nozzle diameter 80 μm. The waterjet speed, V, is calculated by the formula $V = \varphi(2p/\rho_\mathrm{w})^{1/2}$, where p is the waterjet pressure, φ is the coefficient of pressure loss (ranging from 0.95 to 0.99 depending on the nozzle [**2**]) and ρ_w is the density of water. With the characteristic waterjet temperature of 50 °C, the water specific heat is 4174 J/kg K, the density ρ_w is $988.8\,\mathrm{kg/m^3}$, the dynamic viscosity μ is $5.62 \times 10^{-4}\,\mathrm{kg/m\,s}$, the thermal conductivity is 0.664 W/m K and the Prandtl number is 3.64. For a pressure of 50 bar, the speed V is around 100 m/s. Based on the waterjet speed and diameter, the Reynolds number ($Re = \rho_\mathrm{w} V d/\mu$) is about 14 000. The silicon material properties are given in Table 1.

The period during the laser pulse before the material reaches the melting point and is removed is the initiation stage. The penetration stage is characterized by material removal and propagation of the hole boundary. The cooling stage occurs between the end of the laser pulse and the beginning of the next pulse. The numerical solution treats the three stages as parts of a continuous process, but each stage is discussed separately in the following in order to describe the role of the various process parameters.

Table 1 Silicon material properties

Properties	Values
Density	$2330\,\mathrm{kg/m^3}$
Thermal conductivity	Equation (1)
Specific heat	Equations (2a) and (2b)
Melting temperature	1683 K
Latent heat of melting	1.79×10^6 J/kg
Convection heat transfer coefficient	$100\,\mathrm{W/m^2\,K}$
Absorption coefficient (crystalline)	$5.0 \times 10^3\,\mathrm{m}^{-1}$
Surface reflectivity	0.33

5.2.1 *Initiation stage*

The initiation time, or length of the initiation stage, mainly depends on the laser power intensity, surface absorptivity, latent heat of melting and waterjet speed. For the assumed working conditions, the relationship between initiation time and laser power intensity is shown in Fig. 6. Laser power intensities ranging from 0 to $600\,\mathrm{GW/m^2}$ were simulated. Inspection of Fig. 6 reveals that there is a critical value of laser power intensity below which no drilling occurs. For the present case, this critical value is $42.5\,\mathrm{GW/m^2}$. Between this critical value and $100\,\mathrm{GW/m^2}$, the initiation time decreases very rapidly to less than 10 μs. Above a power intensity of $100\,\mathrm{GW/m^2}$, the initiation time decreases very slowly. The full penetration time, which will be discussed in the next section, is also plotted in Fig. 6.

Two specific laser power intensities above the critical value, 75 and $200\,\mathrm{GW/m^2}$, are chosen for the purpose of detailed investigation of the transient temperature profiles. Since the drilling process is symmetric, only the temperatures in a vertical plane through the axis of the laser need be displayed. In Fig. 7, the temperature profiles on the surface are displayed at a series of times during the initiation stage. The surface temperature profiles for 75 and $200\,\mathrm{GW/m^2}$ are shown in

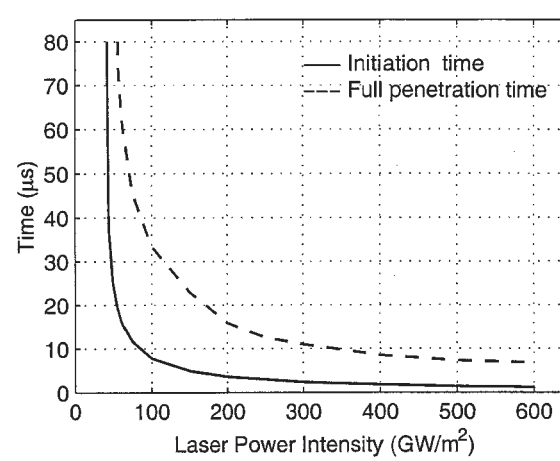

Fig. 6 Initiation and full penetration times versus laser power intensity

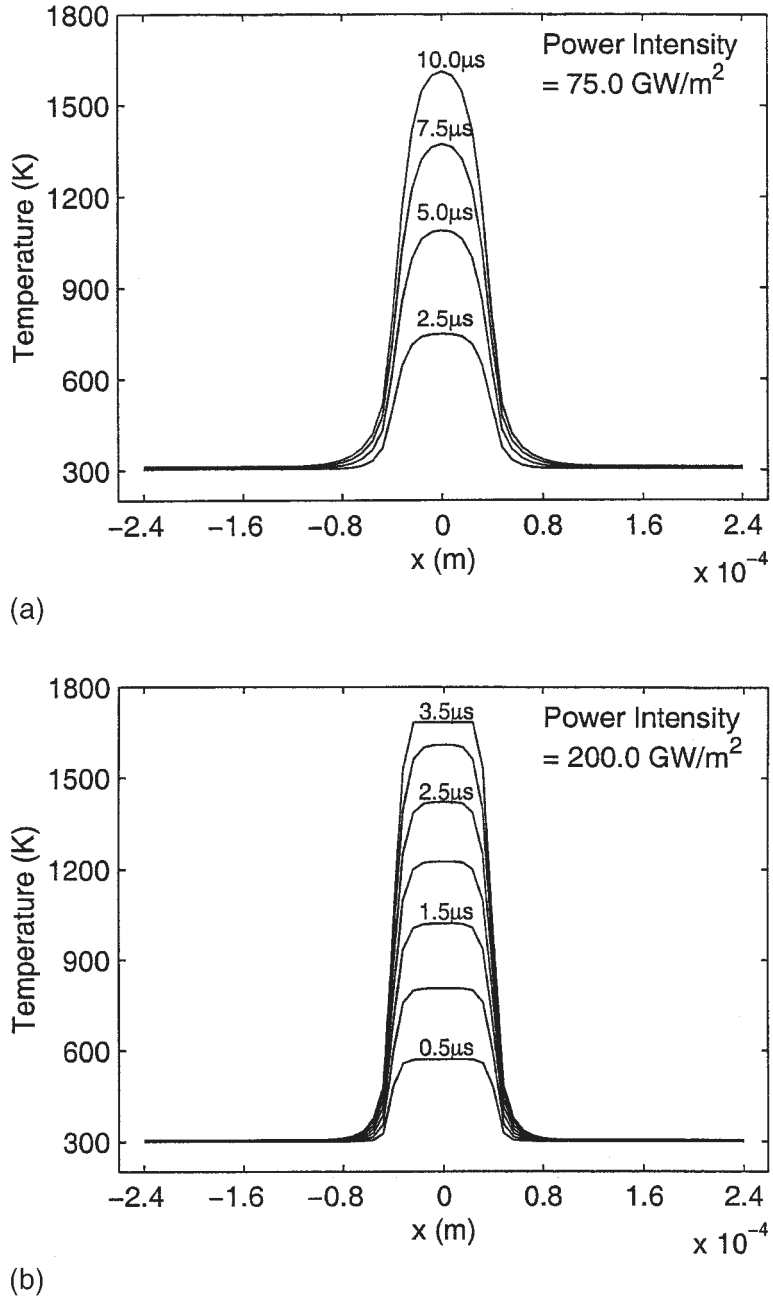

Fig. 7 Surface temperature profiles versus time during the initiation stage: (a) power intensity 75 GW/m^2; (b) power intensity 200 GW/m^2

Figs 7a and b respectively. For the higher power intensity, the surface heats up much more rapidly, and the temperature profile is much flatter in the beam centre area. After only 3.5 μs with a power intensity of 200 GW/m^2, part of the beam centre area reaches the melting temperature of 1683 K, indicated by the temperature plateau near the top of Fig. 7b. The material in this region of the surface will be removed 0.1 μs later at 3.6 μs (see Fig. 6), when the threshold of the latent heat of melting for the associated surface elements is reached. For the lower laser power intensity, no part of the surface has reached the melting temperature even at 10 μs, as shown in Fig. 7a.

The temperature distributions inside the silicon substrate during the initiation stage are shown in Figs 8 and 9. The temperature distributions at 2.5, 5, 7.5 and 10 μs for a power intensity of 75 GW/m^2 are shown in Figs 8a to d. In Fig. 8b it can be seen that a high-temperature region exists just below the surface that is hotter even than the surface. As shown in Fig. 8d, the first points to reach the melting temperature are in this subsurface high-temperature region. This phenomenon was

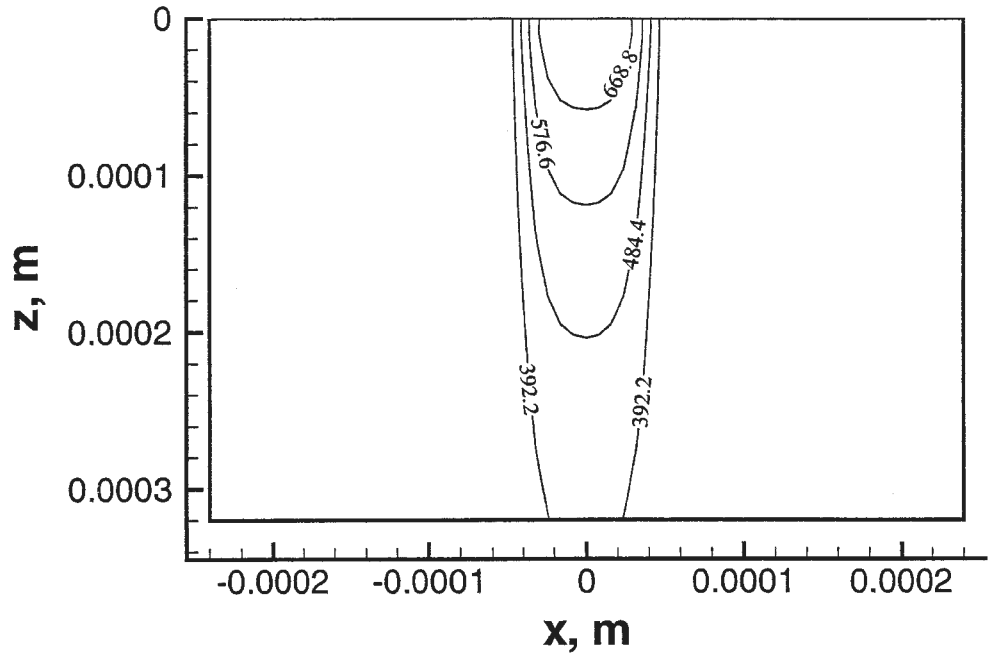

(a)

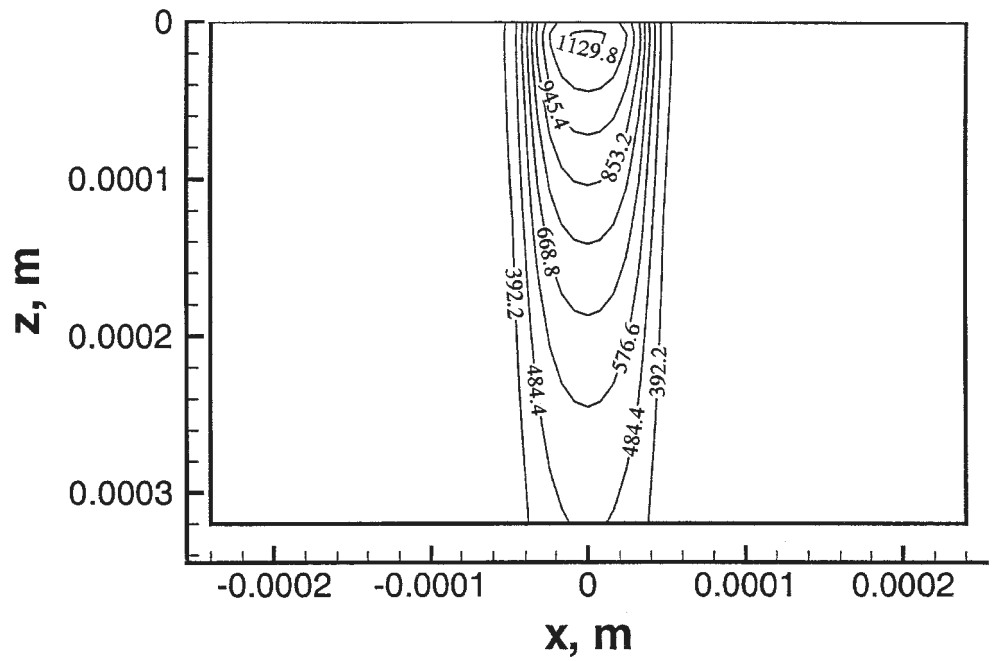

(b)

Fig. 8 (continued over)

observed by Dabby and Paek [**27**], and a mechanism called 'explosive removal of material' was proposed. An explanation given by Blackwell [**28**] is that, before phase change occurs at the surface, the location of the maximum temperature moves inside the workpiece owing to heat losses from the surface to the surroundings. Thus, the material under the surface will melt first. If the material expands during the phase change, explosive material removal could occur. Because of the high cooling effect of the waterjet at the surface, the occurrence of the maximum temperature below the surface is more likely for lower laser power intensities, when the laser power intensity is not sufficient to compensate for the heat loss due to the waterjet. For 75 GW/m^2, the material removal at the surface starts at 11.6 μs (see Fig. 6).

Inspection of Figs 9a to d reveals that the maximum temperature does not occur below the surface for a laser power intensity of 200 GW/m^2. The maximum

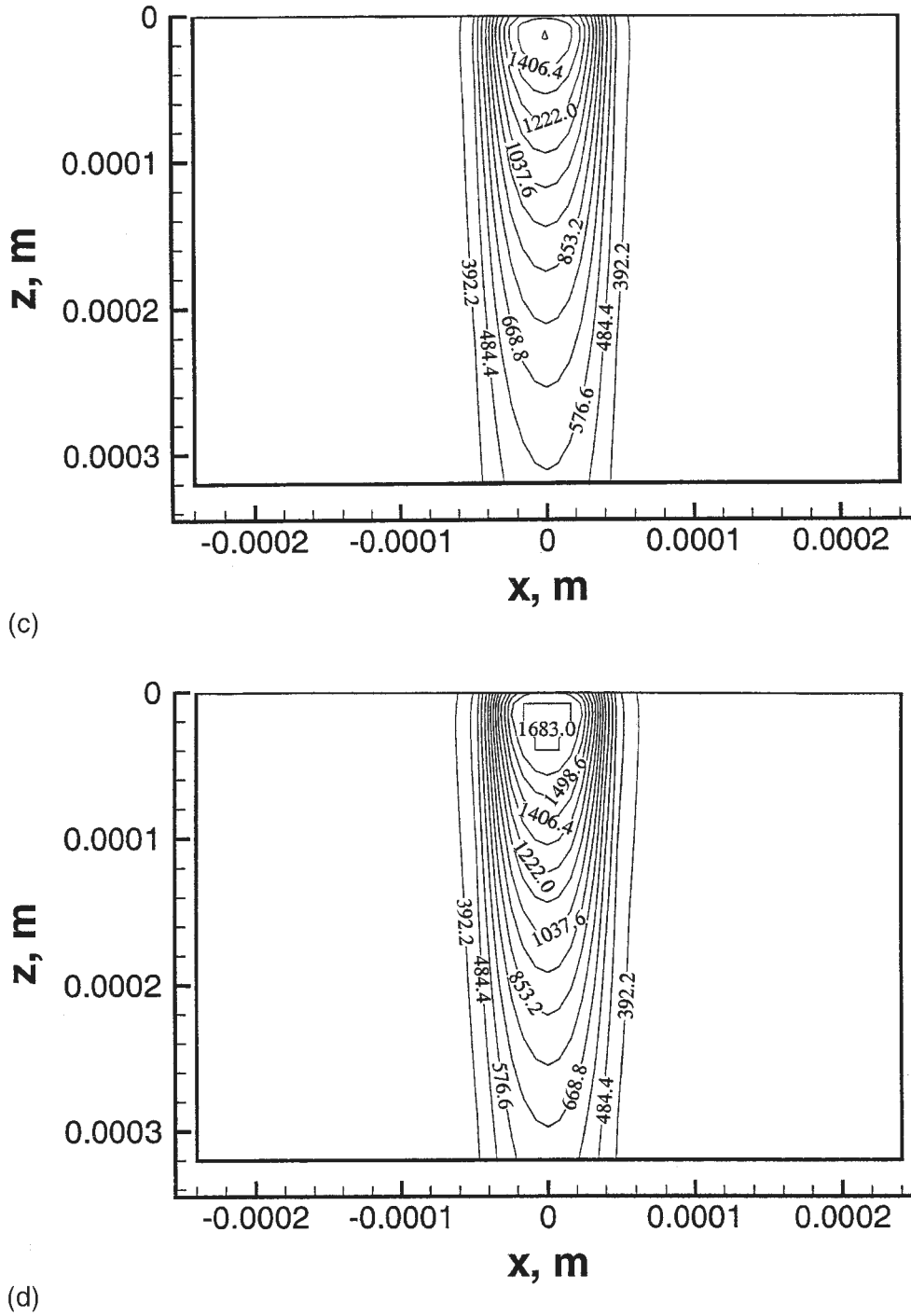

Fig. 8 Temperature distributions during the initiation stage for a power intensity of 75 GW/m^2 at (a) $t = 2.5\,\mu$s, (b) $t = 5.0\,\mu$s, (c) $t = 7.5\,\mu$s and (d) $t = 10.0\,\mu$s

temperature occurs at the surface. In Figs 7 to 9 it can be seen that the heat affected zone is very narrow, only a little wider than the waterjet.

5.2.2 *Penetration stage*

After the latent heat of melting has been accumulated in an element in which the temperature has reached the melting point, the element melts and is removed. The process then enters the penetration stage, during which the boundary of the hole propagates. Different times during the penetration stage for laser power intensities of 75 and 200 GW/m^2 are displayed in Figs 10 and 11 respectively. As shown in Fig. 10a, the hole has progressed about one-third of the way through the workpiece after 20 μs for a power intensity of 75 GW/m^2. After

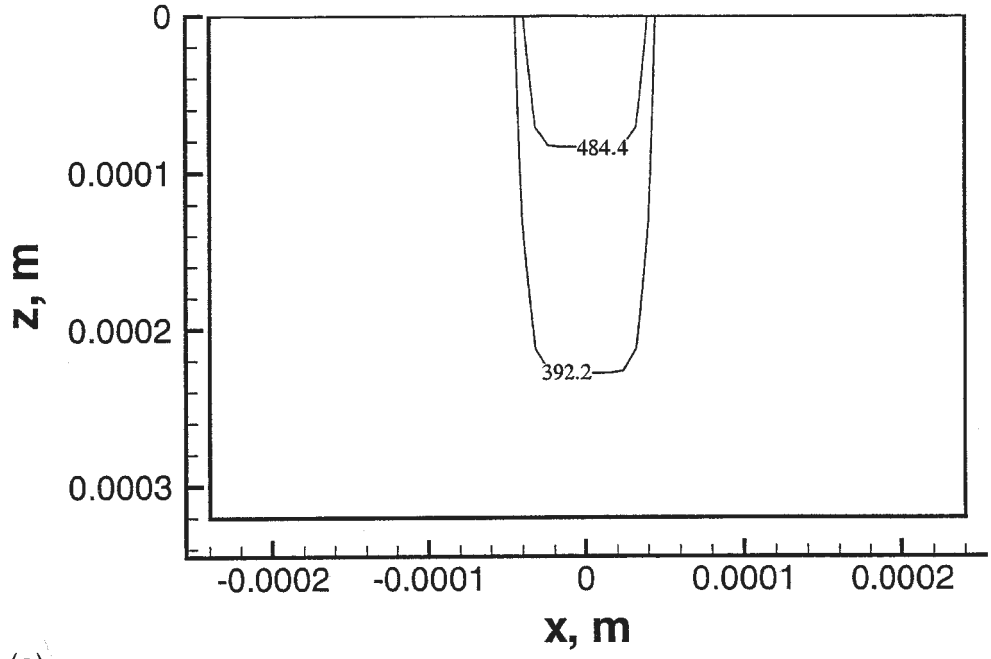

(a)

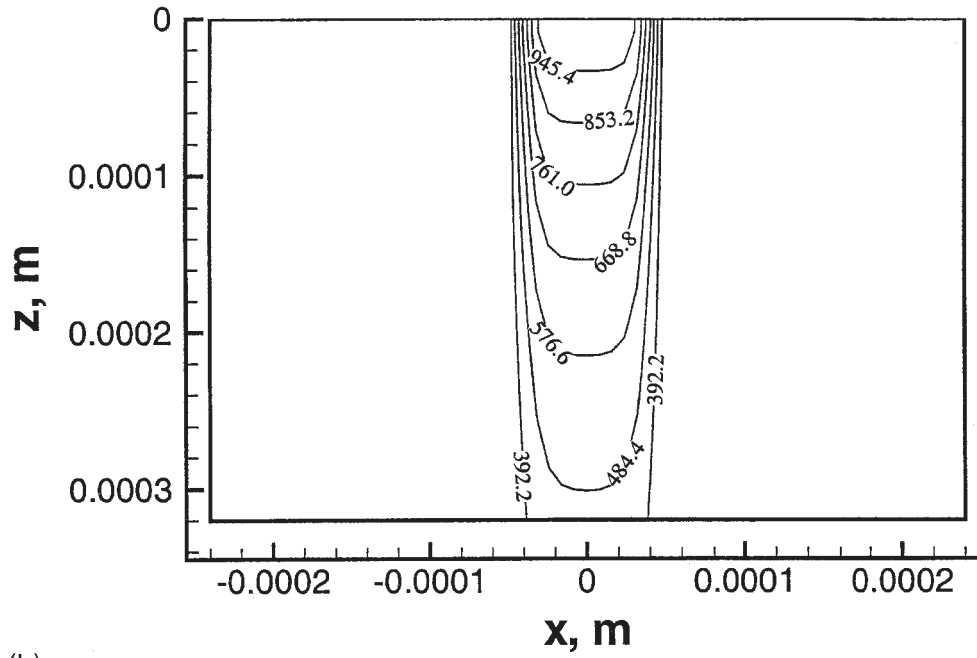

(b)

Fig. 9 (continued over)

40 μs, the hole is most of the way through the workpiece, and it has completely penetrated the workpiece at 80 μs. Although not obvious from Fig. 10, the laser first penetrates the workpiece at 45.4 μs for 75 GW/m^2 (see Fig. 6). From Fig. 11 it can be seen that the hole progresses much more rapidly for the higher laser power intensity. At 10 μs, as shown in Fig. 11b, the hole already has progressed about halfway through the workpiece for a power intensity of 200 GW/m^2. The hole extends completely through the workpiece for 200 GW/m^2 at the full penetration time of 15.9 μs (see Fig. 6). Halfway through the pulse at 40 μs, the hole has vertical sides for the high laser power intensity of 200 GW/m^2 (Fig. 11c), whereas at the end of the pulse at 80 μs the hole sides are still sloped for a low laser power intensity of 75 GW/m^2 (Fig. 10c). The width of the hole is 50 μm for 75 GW/m^2, less than the diameter of the waterjet (80 μm), but it is close to the diameter of the waterjet for 200 GW/m^2. It should also be noted that the hole will not completely penetrate the workpiece within one laser pulse regardless

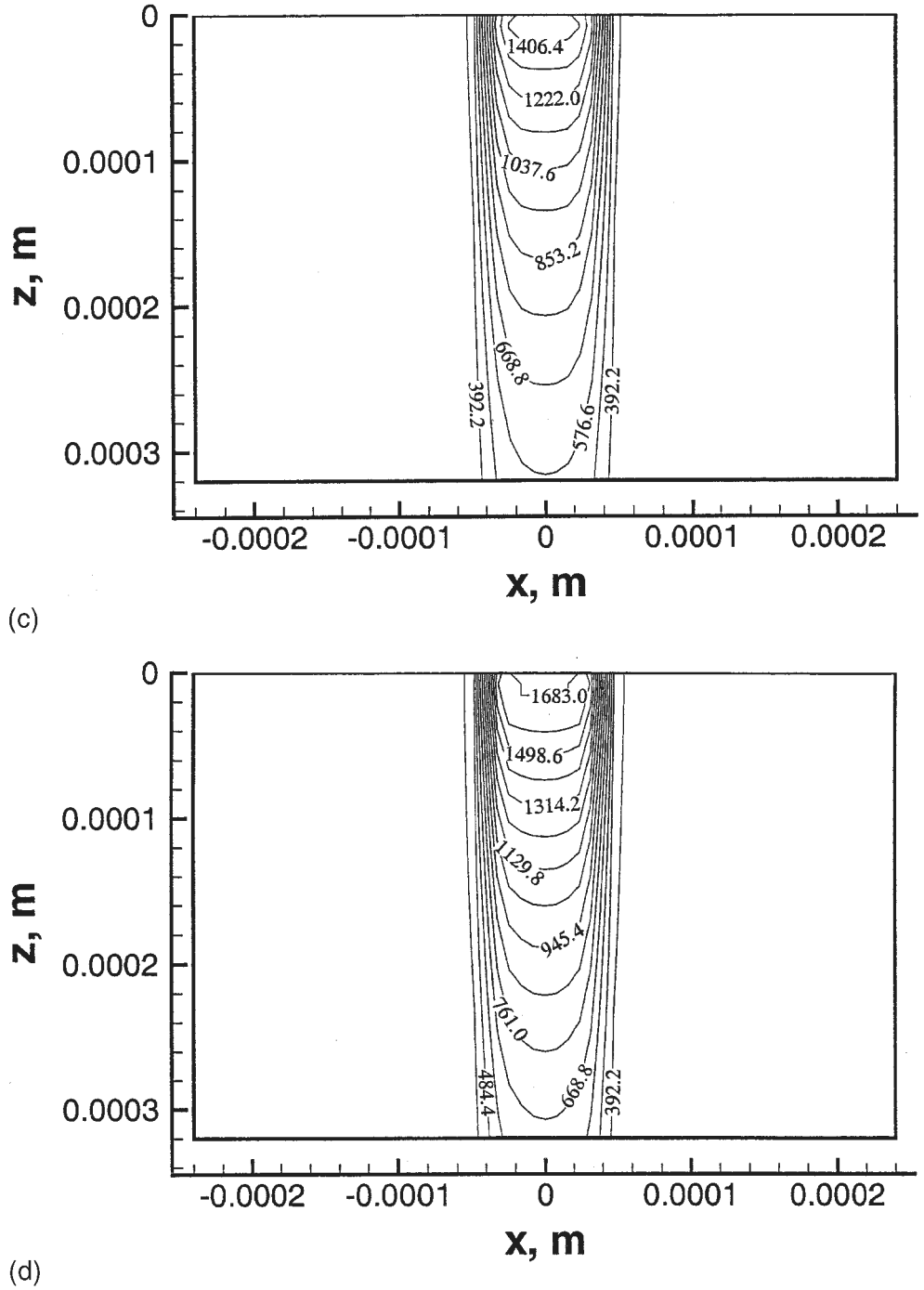

Fig. 9 Temperature distributions during the initiation stage for a power intensity of 200 GW/m^2 at (a) $t = 0.5\,\mu$s, (b) $t = 1.5\,\mu$s, (c) $t = 2.5\,\mu$s and (d) $t = 3.5\,\mu$s

of the time unless the laser power intensity exceeds a critical value, which is 56.5 GW/m^2 for the assumed working conditions. The full penetration times are plotted versus laser power intensity in Fig. 6.

5.2.3 *Cooling stage*

The cooling stage occurs during the interval between the end of one laser pulse and the beginning of the next. The waterjet continues to flow during the cooling phase, rapidly cooling the workpiece. The cooling effect is an important characteristic of waterjet guided laser processing. Indeed, the waterjet cools the workpiece not only during this stage but also throughout the process. This stage is termed the cooling stage because the laser is off and there is no energy input. In Fig. 12, the maximum temperature in the workpiece is plotted versus time. The maximum temperature is 1683 K at 80 μs, which is the time at which the laser pulse ends and the cooling phase begins. As shown in Fig. 12, the maximum

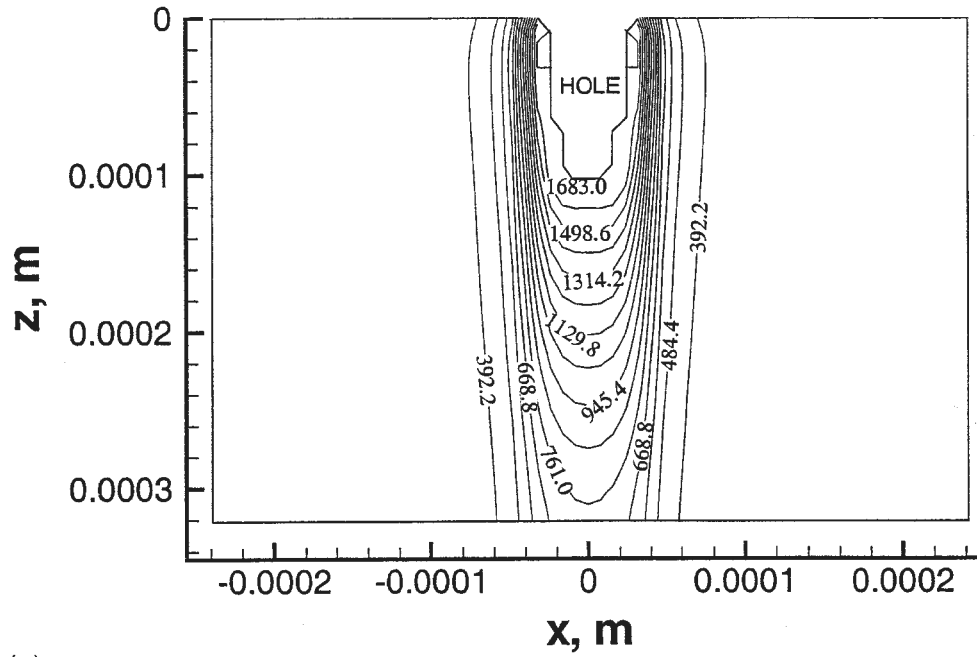

(a)

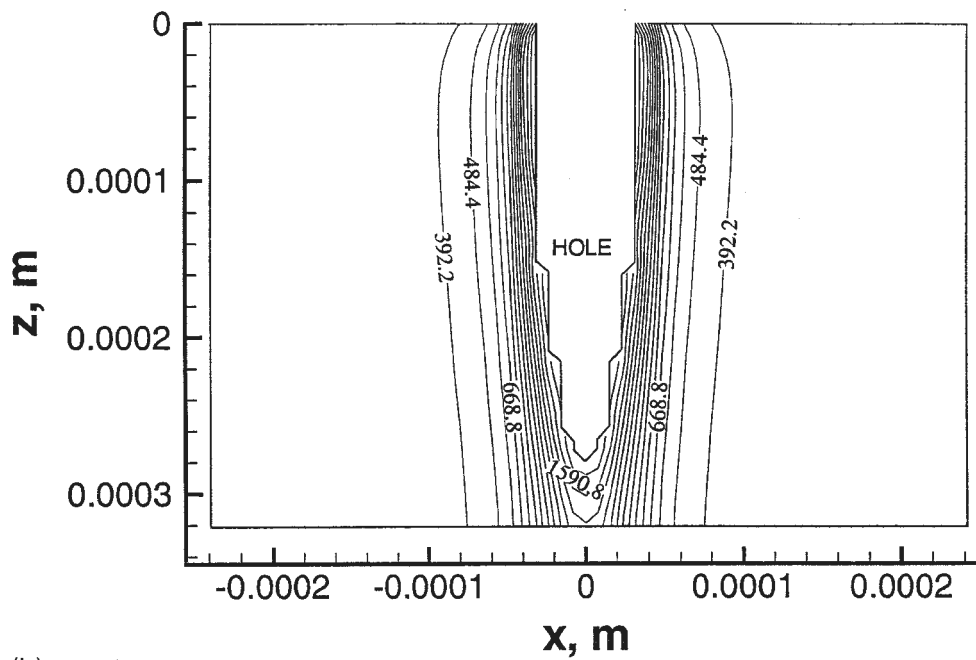

(b)

Fig. 10 (continued over)

temperature drops sharply to about 650 K, between $t = 80\,\mu s$ and $t = 120\,\mu s$, the first 40 μs of the cooling phase. The temperature distribution in the workpiece at 120 μs is shown in Fig. 13.

5.3 Comparison with experimental results

A simulated silicon drilling process with very high pulsating laser power intensity was compared with available experimental results. For the waterjet, the diameter of the nozzle is 50 μm and the waterjet pressure is 300 bar. The thickness of the silicon is 675 μm. For the laser, the pulse length is 0.2 μs and the frequency is 25 000 Hz. The laser output was set at 52 W. The simulation results as well as the experimental results obtained by using the Synova Laser Microjet machine are presented in Fig. 14. In Fig. 14a, the time at which the maximum hole depth is reached, t_m, is plotted versus laser power intensity at the workpiece. The maximum

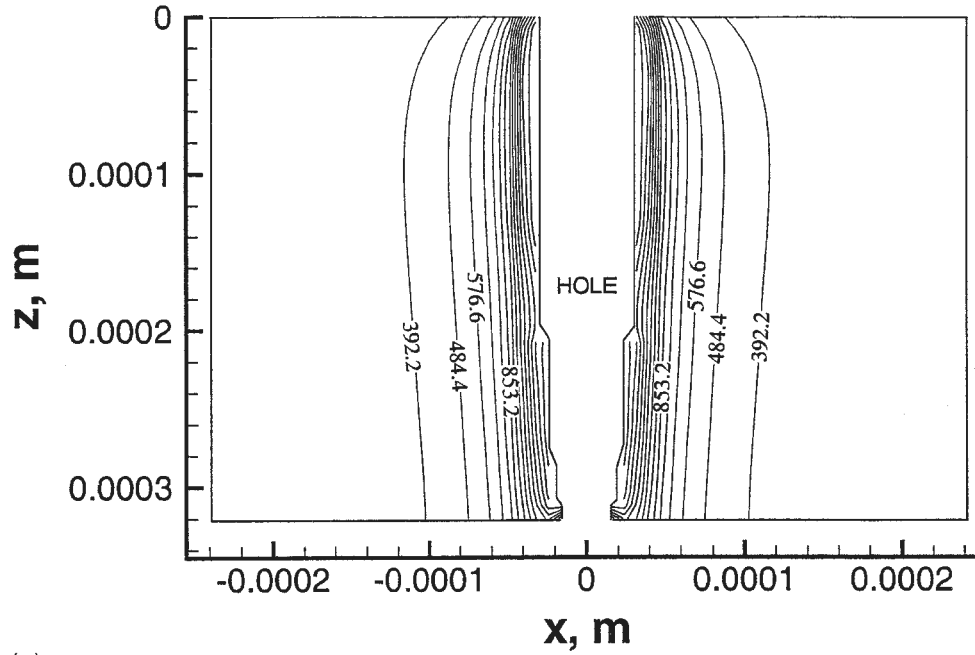

(c)

Fig. 10 Temperature distributions during the penetration stage for a power intensity of 75 GW/m^2 at (a) $t = 20\,\mu$s, (b) $t = 40\,\mu$s and (c) $t = 80\,\mu$s

hole depth, d_m, versus laser power intensity is plotted in Fig. 14b. The experimental data points are represented with asterisks in Fig. 14. Associated with a given laser power intensity is a maximum hole depth. This maximum hole depth is reached at a particular time t_m. Continuing the laser pulses longer than time t_m is ineffective, since there is no increase in the depth of the hole.

The laser power intensity interacting with the workpiece was estimated to be 3.53 TW/m^2 (1 TW/m^2 = 10^{12} W/m^2). At this power intensity, the present simulation produces a maximum hole depth $d_m = 330\,\mu$m at $t_m = 1.4$ ms (35

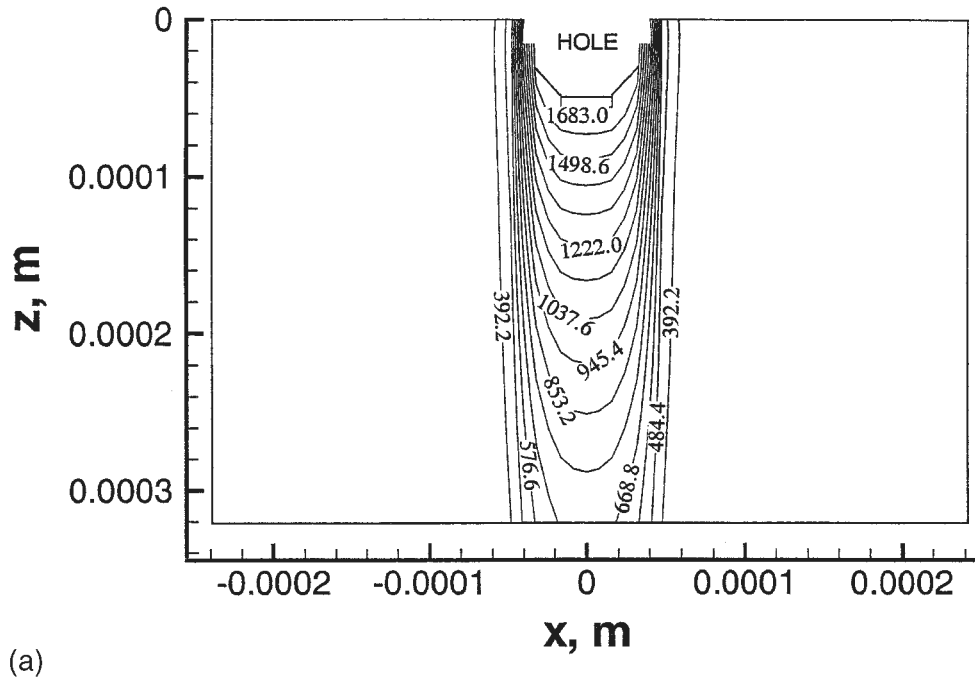

(a)

Fig. 11 (continued over)

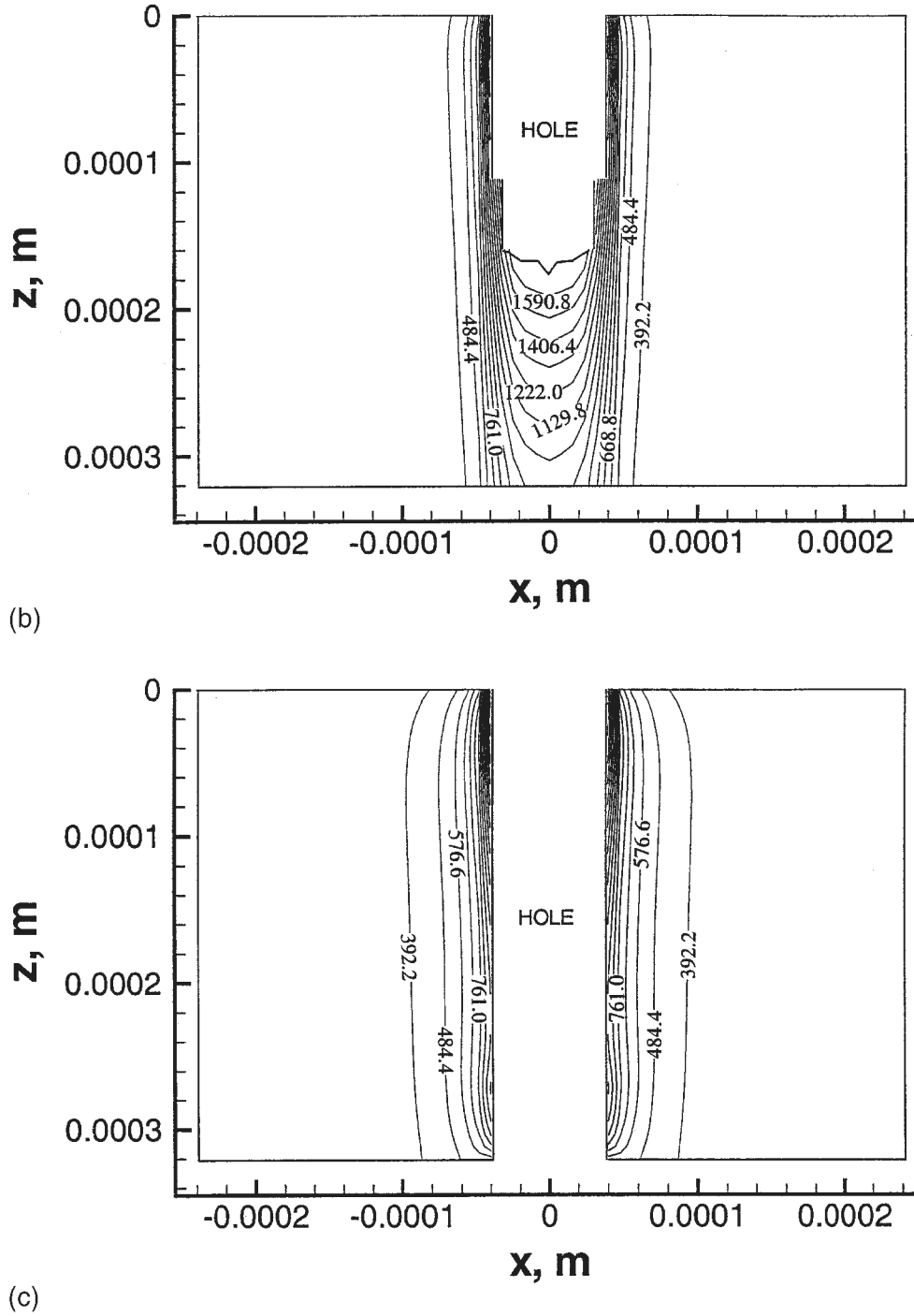

Fig. 11 Temperature distributions during the penetration stage for a power intensity of 200 GW/m^2 at (a) $t = 5\,\mu$s, (b) $t = 10\,\mu$s and (c) $t = 40\,\mu$s

pulses). The experimental results indicate that the hole reaches its maximum depth at $t_m = 1.0$ ms. The simulated and experimental hole cross-sections are shown in Fig. 15. The experimental maximum hole depth obtained from Fig. 15 is about 320 μm. The experimental cross-section was obtained by scribing and then breaking the sample, resulting in some damage to the workpiece and hole. The general shape and depth of the experimental hole are still clearly apparent in Fig. 15. It can be seen that the simulated hole shape is very similar to the experimental shape.

From the simulation results shown in Fig. 14, two observations can be made:

1. When the power intensity is less than 3.21 TW/m^2, no drilling occurs.

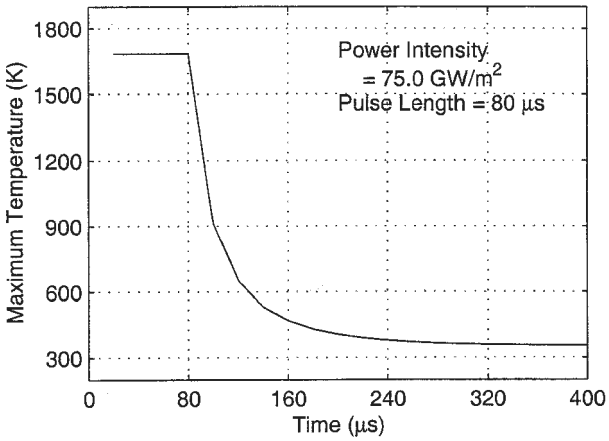

Fig. 12 Maximum workpiece temperature versus time during the cooling stage

2. When the power intensity is between 3.21 and 3.70 TW/m^2, a hole is drilled partially through the workpiece. The power intensity must be higher than 3.70 TW/m^2 in order to drill completely through the workpiece (675 μm).

6 CONCLUSIONS

A model for waterjet guided laser drilling of silicon has been presented, and a simulation based on the model has been developed. The temperature-dependent thermal properties of silicon and the temperature-dependent coupling between the waterjet guided laser and the silicon workpiece have been taken into account. Melting and removal of material as the hole is produced are also accounted for.

The validity of the laser-induced transient heat transfer simulation (without a waterjet) was checked by comparing simulation results with previous published results for the pulsed laser heating of an aluminium workpiece. The predictions of the new simulation were also compared with limited experimental data for waterjet guided laser drilling of silicon, and good agreement was found between simulation results and available experimental results. The new simulation enabled a detailed study of the waterjet guided laser drilling of silicon. The main process characteristics, such as the heat affected zone, temperature field, laser threshold power for drilling and possible subsurface maximum temperatures, were revealed. The three process stages of initiation, penetration and cooling were described.

The details of the flow of the waterjet were not modelled. Further research and additional experimental data are needed to determine the extent to which the process is affected by the complex fluid flow that occurs as the waterjet interacts with a hole extending partially through the workpiece.

ACKNOWLEDGEMENTS

This work was financially supported by the Texas Higher Education Coordinating Board (Project 003656-00189b-1999) and by the US Department of Education (Grant P200A80806-98). The authors would like to thank Dr

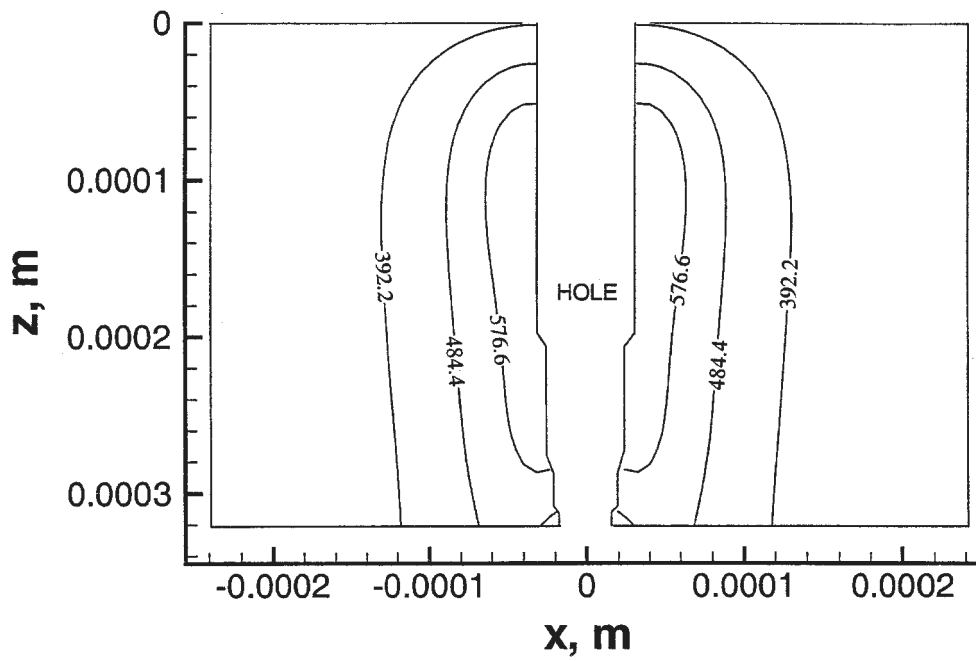

Fig. 13 Temperature distribution 40 μs after the end of the laser pulse for 75 GW/m^2 (t = 120 μs, maximum temperature 649.8 K)

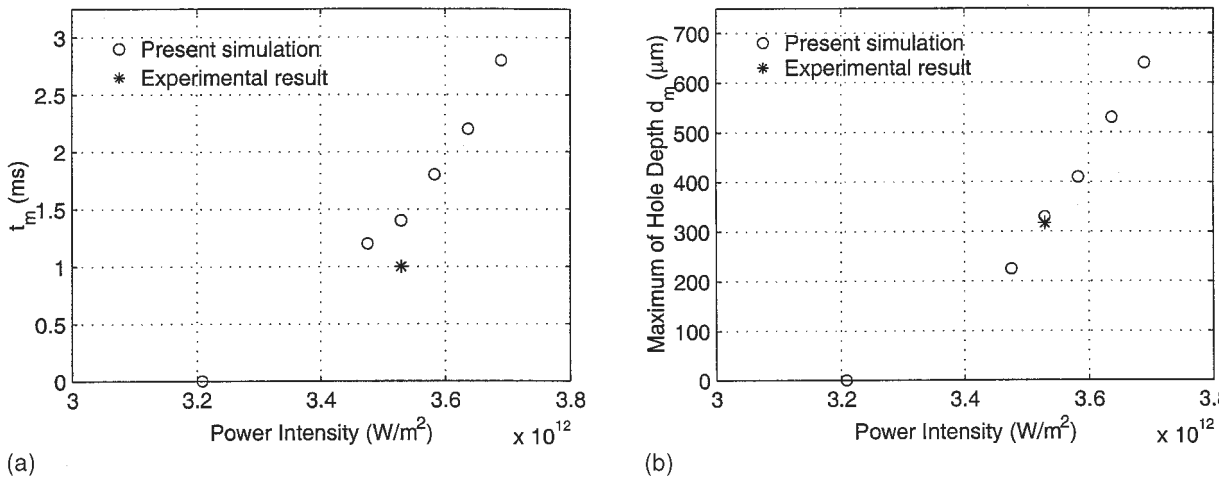

Fig. 14 Comparison between simulated and experimental results: (a) time at which the maximum hole depth is reached versus power intensity; (b) maximum hole depth versus power intensity

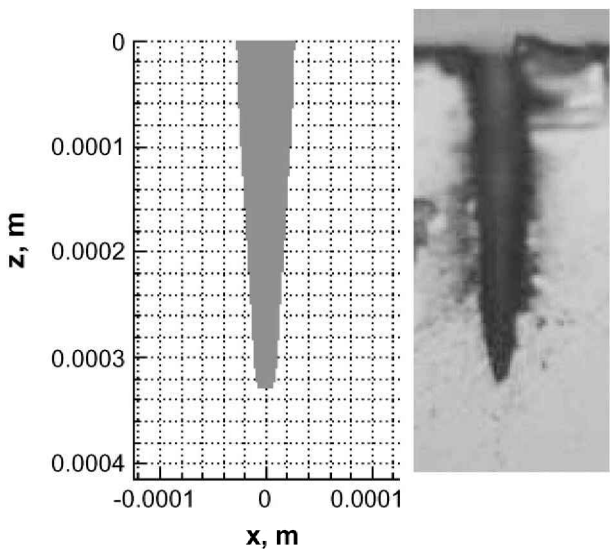

Fig. 15 Comparison between simulated and experimental hole cross-sections

N. Dushkina of The Gem City Engineering Company, Dayton, Ohio, for providing them with the experimental data.

REFERENCES

1 **Richerzhagen, B.** Water-guided laser processing. *Ind. Laser Rev.*, 1997, 8–10.

2 Laser-Microjet—a new method for material processing. SYNOVA Report, Lausanne, Switzerland, 1998.

3 **Wagner, R. E.** Laser drilling mechanics. *J. Appl. Phys.*, 1974, **45**, 4631–4637.

4 **Schuocker, D.** and **Abel, W.** Material removal mechanism of laser cutting. *Proc. SPIE, Ind. Applic. High Power Lasers*, 1983, **455**, 88–95.

5 **Chan, L.** and **Mazumder, J.** One-dimensional steady-state model for damage by vaporization and liquid expulsion due to laser–material interaction. *J. Appl. Phys.*, 1987, **62**, 4579–4586.

6 **Chryssolouris, G.** *Laser Machining: Theory and Practice*, 1991 (Springer, New York).

7 **Gutierrez, G.** and **Jen, T.-C.** Numerical simulation of non-linear heat conduction subjected to a laser source: the effects of variable thermal properties. *Int. J. Heat and Mass Transfer*, 2000, **43**, 2177–2192.

8 **Atanasov, P. A., Eugenieva, E. D.** and **Nedialkov, N. N.** Laser drilling of silicon nitride and alumina ceramics: a numerical and experimental study. *J. Appl. Phys.*, 2001, **89**, 2013–2016.

9 **Armon, E., Zvirin, Y., Laufer, G.** and **Solan, A.** Metal drilling with a CO_2 laser beam. I. Theory. *J. Appl. Phys.*, 1989, **65**, 4995–5002.

10 **Armon, E., Hill, M., Spalding, I. J.** and **Zvirin Y.** Metal drilling with a CO_2 laser beam. II. Analysis of aluminum drilling experiments. *J. Appl. Phys.*, 1989, **65**, 5003–5006.

11 **Diniz Neto, O. O.** and **Lima, C. A. S.** Nonlinear three-dimensional temperature profiles in pulsed laser heated solids. *J. Phys. D: Appl. Phys.*, 1994, **27**, 1795–1804.

12 **Modest, M. F.** Three-dimensional, transient model for laser machining of ablating/decomposing materials. *Int. J. Heat and Mass Transfer*, 1996, **39**, 221–234.

13 **Cheng, C. F., Tsui, Y. C.** and **Clyne, T. W.** Application of a three-dimensional heat flow model to treat laser drilling of carbon fibre composites. *Acta Mater.*, 1998, **46**, 4273–4285.

14 **Zhang, Y. W.** and **Faghri, A.** Vaporization, melting and heat conduction in the laser drilling process. *Int. J. Heat and Mass Transfer*, 1999, **42**, 1775–1790.

15 **Xu, X., Grigoropoulos, C. P.** and **Russo, R. E.** Heat transfer in excimer-laser melting of thin polysilicon layers. *Trans. ASME, J. Heat Transfer*, 1995, **117**, 708–715.

16 **Grigoropoulos, C. P., Buckholz, R. H.** and **Domoto, G. A.** A heat-transfer algorithm for the laser-induced melting and recrystallization of thin silicon layers. *J. Appl. Phys.*, 1986, **60**, 2304–2309.

17 **Schvan, P.** and **Thomas, R. E.** Time-dependent heat flow calculation of cw laser-induced melting of silicon. *J. Appl. Phys.*, 1985, **57**, 4738–4741.

18 **Holman, J. P.** *Heat Transfer*, 9th edition, 2002 (McGraw-Hill, New York).

19 **Patankar, S. V.** *Numerical Heat Transfer and Heat Flow*, 1980 (McGraw-Hill, New York).

20 **Patankar, S. V.** A numerical method for conduction in composite materials, flow in irregular geometries and conjugate heat transfer. In 6th International Heat Transfer Conference, Toronto, Canada, 1978, Vol. 3, pp. 297–302.

21 **Mazumder, J.** and **Steen, W. M.** Heat transfer model for cw laser material processing. *J. Appl. Phys.*, 1980, **51**, 941–947.

22 **Gardon, R.** and **Cobonpue, J.** Heat transfer between a flat plate and jets of air impinging on it. International Heat Transfer Conference, 1961, Part II, pp. 454–460.

23 **Elison, B.** and **Webb, B. W.** Local heat-transfer to impinging liquid jets in the initially laminar, transitional, and turbulent regimes. *Int. J. Heat and Mass Transfer*, 1994, **37**, 1207–1216.

24 **Stevens, J.** and **Webb, B. W.** Local heat transfer coefficients under axisymmetric, single-phase liquid jet. *Trans. ASME, J. Heat Transfer*, 1991, **113**, 71–78.

25 **Sun, H., Ma, C.-F.** and **Chen, Y. C.** Prandtl number dependence of impingement heat transfer with circular free-surface liquid jets. *Int. J. Heat and Mass Transfer*, 1998, **41**, 1360–1363.

26 **Webb, B. W.** and **Ma, C.-F.** Single-phase liquid jet impingement heat transfer. *Adv. Heat Transfer*, 1995, **26**, 105–217.

27 **Dabby, F. W.** and **Paek, U.** High-intensity laser-induced vaporization and explosion of solid materials. *IEEE J. Quantum Electronics*, 1972, **QE-8**(2), 106–111.

28 **Blackwell, B. F.** Temperature profile in semi-infinite body with exponential source and convective boundary condition. *Trans. ASME, J. Heat Transfer*, 1990, **112**, 567–571.